Original Article

Characterization of microvessels and parenchyma in in-line phase contrast imaging CT: healthy liver, cirrhosis and hepatocellular carcinoma

Jinghao Duan[1,2], Chunhong Hu[3], Qingtao Qiu[2], Jing Zhang[2], Huipeng Meng[4], Keqiang Wang[4], Huajiang Dong[4], Hong Wei[2], Yong Yin[2]

[1]School of Precision Instrument and Opto-electronics Engineering, Tianjin University, Tianjin 300072, China; [2]Department of Radiation Oncology, Shandong Cancer Hospital and Institute, Shandong First Medical University and Shandong Academy of Medical Sciences, Ji'nan 250117, China; [3]College of Biomedical Engineering, Tianjin Medical University, Tianjin 300070, China; [4]State Key Laboratory of Precision Measurement Technology and Instruments, Tianjin University, Tianjin 300072, China

Correspondence to: Yong Yin, PhD. Department of Radiation Oncology, Shandong Cancer Hospital and Institute, Shandong First Medical University and Shandong Academy of Medical Sciences, Ji'nan 250117, China. Email: yinyongsd@126.com.

Background: Hepatocellular carcinoma (HCC) is a cancer with a poor prognosis, and approximately 80% of HCC cases develop from cirrhosis. Imaging techniques in the clinic seem to be insufficient for revealing the microstructures of liver disease. In recent years, phase contrast imaging CT (PCI-CT) has opened new avenues for biomedical applications owing to its unprecedented spatial and contrast resolution. The aim of this study was to present three-dimensional (3D) visualization of human healthy liver, cirrhosis and HCC using a PCI-CT technique called in-line phase contrast imaging CT (ILPCI-CT) and to quantitatively evaluate the variations of these tissues, focusing on the liver parenchyma and microvasculature.

Methods: Tissue samples from 9 surgical specimens of normal liver (n=3), cirrhotic liver (n=2), and HCC (n=4) were imaged using ILPCI-CT at the Shanghai Synchrotron Radiation Facility (SSRF) without contrast agents. 3D visualization of all *ex vivo* liver samples are presented. To quantitatively evaluate the vessel features, the vessel branch angles of each sample were clearly depicted. Additionally, radiomic features of the liver parenchyma extracted from the 3D images were measured. To evaluate the stability of the features, the percent coefficient of variation (%COV) was calculated for each radiomic feature. A %COV <30 was considered to be low variation. Finally, one-way ANOVA, followed by Tukey's test, was used to determine significant changes among the different liver specimens.

Results: ILPCI-CT allows for a clearer view of the architecture of the vessels and reveals more structural details than does conventional radiography. Combined with the 3D visualization technique, ILPCI-CT enables the acquisition of an accurate description of the 3D vessel morphology in liver samples. Qualitative descriptions and quantitative assessment of microvessels demonstrated clear differences among human healthy liver, cirrhotic liver and HCC. In total, 38 (approximately 51%) radiomic features had low variation, including 11 first-order features, 16 GLCM features, 6 GLRLM features and 5 GLSZM features. The differences in the mean vessel branch angles and 3 radiomic features (first-order entropy, GLCM-inverse variance and GLCM-sum entropy) were statistically significant among the three groups of samples.

Conclusions: ILPCI-CT may allow for morphologic descriptions and quantitative evaluation of vessel microstructures and parenchyma in human healthy liver, cirrhotic liver and HCC. Vessel branch angles and radiomic features extracted from liver parenchyma images can be used to distinguish the three kinds of liver tissues.

Keywords: In-line phase contrast imaging CT (ILPCI-CT); synchrotron radiation; hepatocellular carcinoma (HCC); cirrhosis; radiomic features

Submitted Dec 09, 2018. Accepted for publication Jun 17, 2019.
doi: 10.21037/qims.2019.06.12
View this article at: http://dx.doi.org/10.21037/qims.2019.06.12

Introduction

Hepatocellular carcinoma (HCC) is the sixth most prevalent cancer in the world and usually has a poor prognosis (1). Cirrhosis with various etiologies is deemed to be the most important clinical risk factor for HCC, with approximately 80% of HCC cases developing in patients with cirrhosis (2). The multistep process of transitioning from a healthy liver to a cirrhotic liver and then to HCC is characterized by a series of alterations in the liver parenchyma and vessels (3). The detection and analysis of these changes, especially in fine structures, therefore seems to be critical to improving the understanding of the development of HCC.

In current clinical practice, an invasive biopsy technique is still serving as the gold standard for the assessment of hepatic diseases (4). However, the drawbacks of this approach are worthy of mention (5). First, the spatial and temporal pathologic status limits the ability of invasive biopsy techniques to fully capture their state. Furthermore, the necessity of repeated and invasive sampling may be burdensome to the patient and limits the practical number of opportunities to monitor disease progression and the treatment response. Therefore, a noninvasive, consistent, precise, and repeatable method of evaluating these lesions should be developed.

As a noninvasive technique, medical imaging can be performed with low risk to and convenience for the patient. It can provide a comprehensive macroscopic picture of miscellaneous disorders, which is ideally suited for diagnosis, staging, treatment planning, and response assessment. Among existing imaging techniques, ultrasound (US), computed tomography (CT) and magnetic resonance (MR) imaging have been researched for the noninvasive detection and characterization of the multistep process of hepatocarcinogenesis (6). They can provide vivid liver parenchyma and vessel images with a spatial resolution reaching 0.5 mm, particularly when using contrast agents. However, for CT images, their ability to distinguish weakly absorbing tissues is far less that desirable, despite the resolution of CT images being superior to that of other imaging technologies. Therefore, medical imaging techniques in the clinic are not sufficient for characterizing some lesions due to insufficient contrast and spatial resolution.

To overcome the above challenges, phase contrast imaging (PCI) characterized by high sensitivity and good soft-tissue contrast has been used in biomedical imaging (7-10). By measuring the phase shift of X-rays that occur when passing through an object, the technique has approximately 1,000-fold greater sensitivity than absorption for low-atomic number elements such as carbon, hydrogen and oxygen (11). The technique has also been introduced into X-ray computed tomography. Phase contrast imaging CT (PCI-CT) can acquire the three-dimensional (3D) morphology of microstructures in biomedical samples. It overcomes the limitations of overlapping liver structures, making it possible to render hepatic structures with 3D visualization (12,13).

Over the last few years, several applied approaches for such imaging have been reported for the brain (14,15), spinal cord (16-18), lung (19,20), breast (21), liver (22-24), kidney (25), etc. In our previous studies, we found PCI-CT could clearly detect the hepatic sinusoids in human cavernous hemangioma samples (26). Additionally, we found that PCI-CT allows for the visualization and depiction of various stages of liver fibrosis in rats without the need for a contrast agent (27). For PCI-CT experiments involving human liver disease, however, few studies have been reported, although a few trials involving other human tissues are ongoing in synchrotron facilities.

Therefore, the aim of this study was to present three-dimensional (3D) visualization of human healthy liver, cirrhotic liver and HCC using the PCI-CT technique and to quantitatively evaluate the variations of these tissues, focusing on the liver parenchyma and microvasculature.

Methods

Tissue samples preparation

Tissue samples from 9 surgical specimens of normal liver (n=3), cirrhotic liver (n=2), and HCC (n=4) were obtained from Tianjin Medical University Cancer Institute and Hospital. Informed consent was obtained from all patients, and the local ethics board approved the study protocol (Tianjin Medical University Cancer Institute and

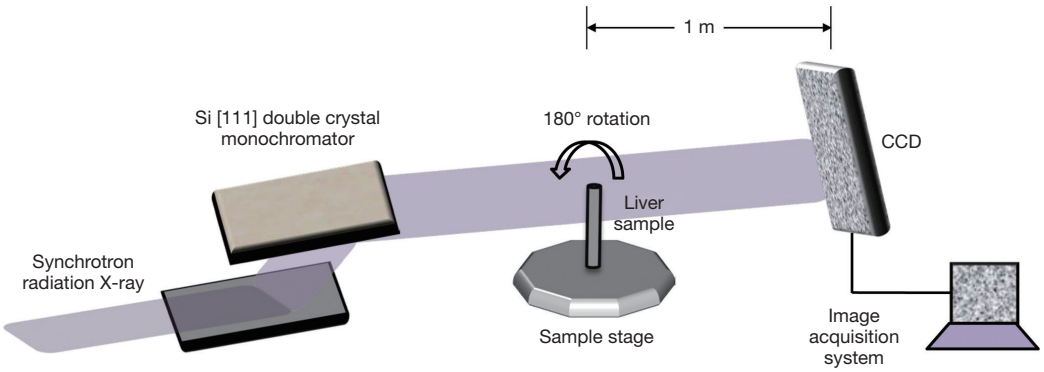

Figure 1 Schematic diagram of the ILPCI set-up at BL13W1 in SSRF. ILPCI, in-line phase contrast imaging.

Table 1 The experimental parameters used in ILPCI

Experimental parameters	ILPCI
Scanning energy (keV)	16
Sample-to-detector distance (m)	1
Exposure time (ms)	75
CCD (μm pixel^{-1})	9
Projection images number	1,200
Flat field images number	10
Dark field images number	20

ILPCI, in-line phase contrast imaging.

the hospital ethics committee). The samples removed at hepatectomy were preserved in 10% buffered formalin within half an hour. Prior to imaging, the samples were cut into small pieces (8 mm in height and approximately 5 mm in diameter). During CT imaging, the specimens were sealed in cylindrical polyethylene containers that were 8 mm in diameter.

Phase contrast imaging CT and imaging acquisition

PCI and absorption imaging were performed using an X-ray imaging and biomedical application beamline (BL13W1) at the Shanghai Synchrotron Radiation Facility (SSRF) in China (*Figure 1*). BL13W1 employs the in-line phase contrast imaging CT (ILPCI-CT) method with a high flux density of 3rd generation synchrotron radiation. A detailed description of ILPCI-CT can be found in a previous study (26). In this experiment, first we obtained planar images, including attenuation-contrast images and phase contrast images of the same specimens that were mounted on the rotation stage controlled by a precise step motor. Then, in a tomography scan, for each sample, a total of 1,200 projection images were generated from different angular directions when the samples were rotated within 180°. In addition, 20 flat field images (with no sample in the beam) were recorded to normalize the image intensity. In addition, 10 dark field images, which were recorded when no photons hit the detector, were also collected to correct for the detector's dark current offset. The experimental parameters used for ILPCI-CT in this study are provided in *Table 1*.

Image reconstruction and 3D visualization

Before the image reconstruction operation, the regions of interest (ROIs), which included the whole liver samples, were first selected from the projection images to avoid massive data and to save computation time. The ROIs were stored as images of 1,500×400 pixels. Then, the images were subjected to flat field and dark field correction. Finally, the raw data were processed by applying the standard filter back-projection (FBP) algorithm (28) with MATLAB software (MATLAB 2014a, MathWorks, Natick, Massachusetts, USA). To highlight the edge of the vessels, image enhancement was used after ring artifact correction. Using 3D visualization software (Amira; Visage Imaging, Berlin, Germany), a surface rendering method was applied to visualize the vessel microstructures, which allowed for a clear depiction of the anatomical and pathological vessels and provided a strong space sense.

Image analysis and quantitative assessment

In the multistep process of hepatocarcinogenesis, the liver parenchyma is destroyed continuously as characterized by

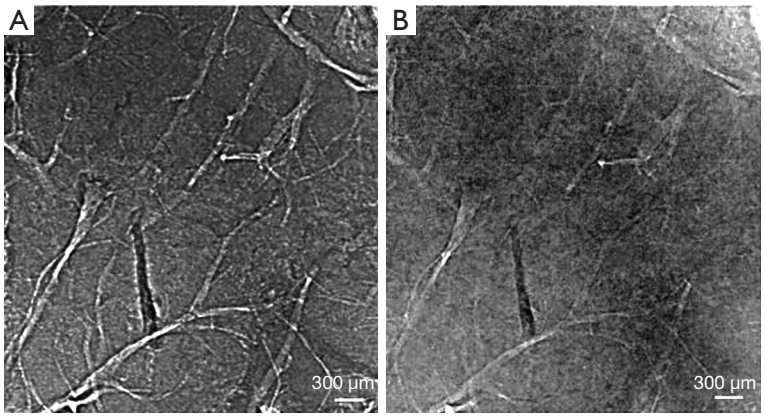

Figure 2 Planar X-ray images of one healthy liver sample. (A) PCI projection image; (B) conventional radiograph. PCI, phase contrast imaging.

texture alterations. In this study, we quantitatively assessed the variations through analyzing the radiomic features of the liver parenchyma in the ILPCI-CT 3D images. For each sample, using 3D Slicer software (www.slicer.org), 5 cylindrical volumes of interest (VOIs) approximately 40 pixels in height and 60 pixels in diameter were defined in the parenchyma, avoiding vessels. All radiomic feature calculations for each VOI were performed using the Radiomics extension in 3D Slicer software, which is a publicly available and easily accessible software and can be employed for high-throughput data mining research of medical imaging.

In total, we obtained 45 VOIs including 15 VOIs from healthy liver samples, 10 VOIs from cirrhotic liver samples and 20 VOIs from HCC samples. For each VOI, we extracted 74 radiomic features including 19 first-order statistical features and 55 textural features. To evaluate the stability of the features, the percent coefficient of variation (%COV) was calculated for each radiomic feature in this paper, and %COV <30 was considered to be low variation. The definition of %COV is as follows (29):

$$\%COV = \frac{S.D}{Mean} \times 100$$

where *S.D* and *Mean* represent the standard deviation and mean value of the radiomic feature.

In general, the morphology and structure of the microvasculature could be changed along with the process of hepatocarcinogenesis. After performing a CT reconstruction operation, we acquired the 3D image data sets. Then, 3D visualization of the microvessels was created using the isosurface module in Amira v6.0.1 software (FEI Visualization Science Group, Burlington, MA). Applied to the 3D images, the isosurface module is efficient for providing an impression of the 3D shape of the microvessels. In this process, to decrease computation time and improve rendering performance, we employed resampling for the 3D image data sets. Then, we adjusted the threshold port to obtain the 3D visualization results of the microvessels. Finally, measurement of the vessel branch angles was performed using the 3D angle tool in Amira.

Statistical analyses

Statistical analyses were performed by one author using SPSS software (version 20; IBM, Chicago, USA). All measurements are expressed as means ± standard deviations and were subjected to analysis of variance (ANOVA) among groups. We conducted comparisons of the three groups using one-way ANOVA followed by Tukey's test, and for comparisons involving two groups, we used an unpaired *t* test. Differences were considered statistically significant when P values were <0.05.

Results

ILPCI planar imaging

Figure 2A shows the ILPCI planar image of one healthy liver sample, and the architecture of the vessel is clearly visualized. In contrast, vessel trees are relatively indistinct in the conventional radiograph image of the same specimen (*Figure 2B*).

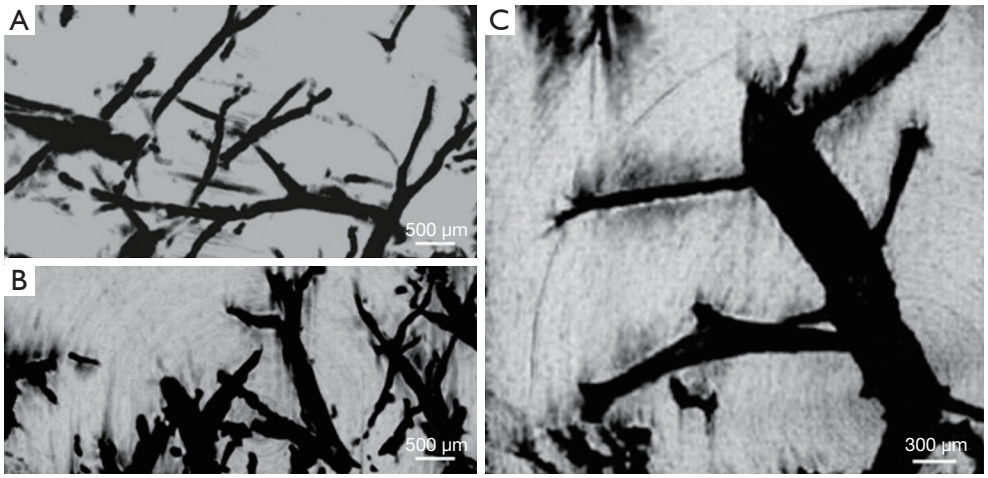

Figure 3 ILPCI-CT MIP images of different liver samples. (A) Healthy liver MIP image; (B) cirrhotic liver MIP image; (C) HCC MIP image. ILPCI, in-line phase contrast imaging; MIP, maximum intensity projection; HCC, hepatocellular carcinoma.

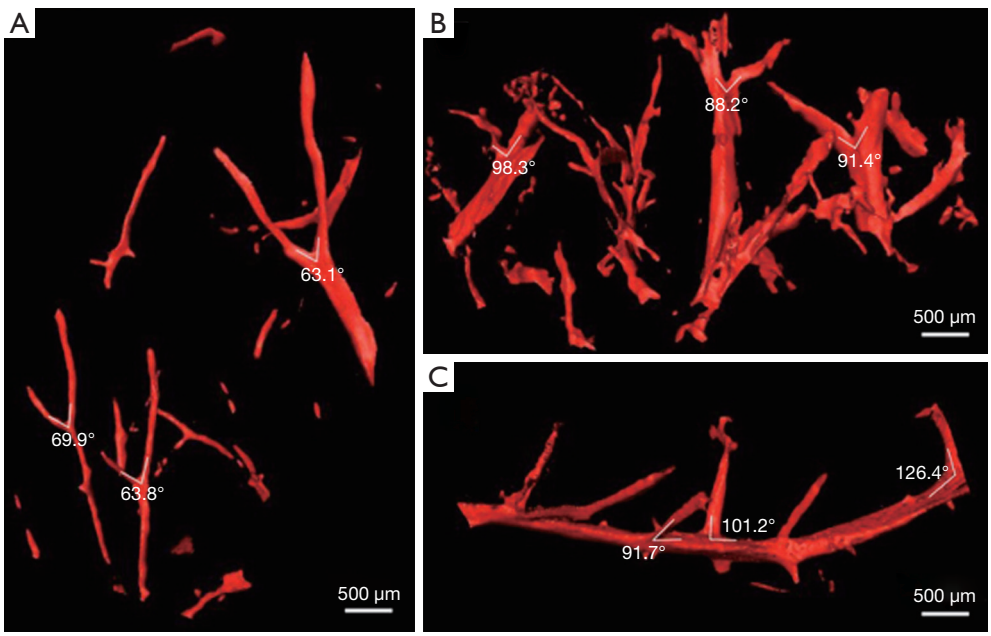

Figure 4 3D microvascular structures visualization of different liver samples. (A) Healthy liver 3D microvascular structures; (B) cirrhotic liver 3D microvascular structures; (C) HCC 3D microvascular structures. Measurements of several vessel branch angles for different liver samples is displayed in this figure. CC, hepatocellular carcinoma.

Maximum intensity projection (MIP) images and 3D microvascular structures visualization

Figures 3A, *B* and *C* show the MIP images of the healthy liver, cirrhotic liver and HCC samples, respectively. The microvascular and parenchyma sections are shown clearly. In *Figure 4*, 3D visualization of different liver samples is presented with vivid shapes and stereoscopic effects. The vessel trend and branches in the healthy liver sample (*Figure 4A*) appear ordered and regular without obvious vascular abnormalities. The vessel walls are also quite smooth. In *Figure 4B*, due to the compression caused by fibrosis, the vessel appears stiffer and as a 'dry stick' in the

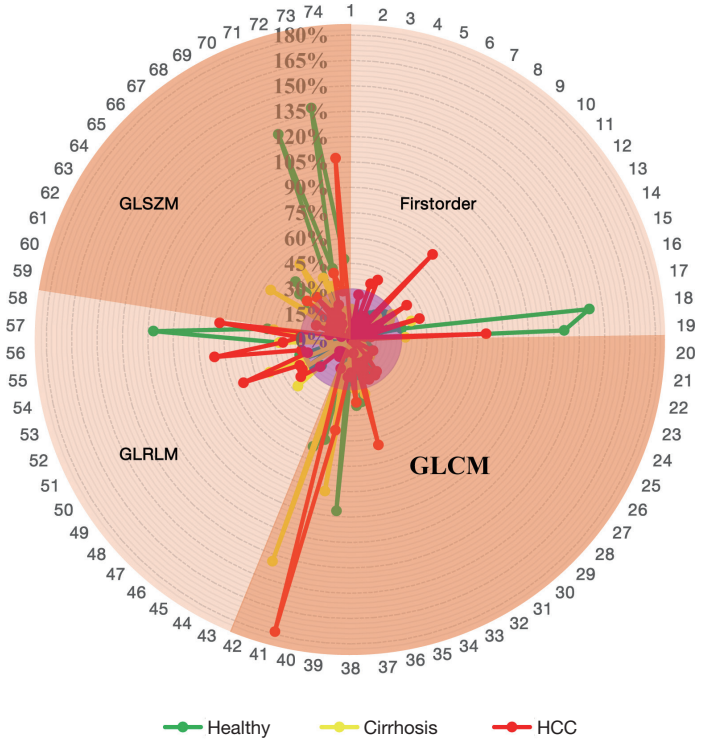

1-Maximum*
2-Range*
3-10Percentile*
4-Mean*
5-RootMeanSquared
6-Median
7-90Percentile*
8-Kurtosis*
9-Entropy*
10-Minimum
11-Uniformity*
12-RobustMeanAbsoluteDeviation*
13-InterquartileRange
14-MeanAbsoluteDeviation*
15-StandardDeviation*
16-Variance
17-Skewness
18-TotalEnergy
19-Energy
20-Idmn*
21-Idn*
22-InverseVariance*
23-Id*
24-Idm*
25-DifferenceEntropy*
26-SumEntropy*
27-Entropy*
28-SumAverage*
29-AverageIntensity*
30-Dissimilarity*
31-MaximumProbability*
32-DifferenceVariance*
33-Energy*
34-Contrast*
35-SumSquares
36-Autocorrelation
37-Imc2
38-SumVariance*
39-Correlation
40-Imc1
41-ClusterProminence
42-ClusterShade
43-RunEntropy*
44-ShortRunEmphasis*
45-RunPercentage*
46-RunLengthNonUniformityNormalized*
47-GrayLevelNonUniformityNormalized*
48-ShortRunLowGrayLevelEmphasis
49-LowGrayLevelRunEmphasis
50-GrayLevelVariance
51-HighGrayLevelRunEmphasis
52-LongRunHighGrayLevelEmphasis
53-ShortRunHighGrayLevelEmphasis
54-LongRunEmphasis*
55-RunVariance
56-LongRunLowGrayLevelEmphasis
57-GrayLevelNonUniformity
58-RunLengthNonUniformity
59-ZoneEntropy*
60-SmallAreaEmphasis*
61-GrayLevelNonUniformityNormalized*
62-SizeZoneNonUniformityNormalized*
63-SmallAreaLowGrayLevelEmphasis
64-GrayLevelVariance
65-LowGrayLevelZoneEmphasis
66-HighGrayLevelZoneEmphasis
67-SmallAreaHighGrayLevelEmphasis
68-GrayLevelNonUniformity
69-ZonePercentage*
70-SizeZoneNonUniformity
71-LargeAreaLowGrayLevelEmphasis
72-LargeAreaEmphasis
73-ZoneVariance
74-LargeAreaHighGrayLevelEmphasis

Figure 5 The %COV value of different radiomic features. The correspondence between numbers and features is shown on the right. *, represents the %COV value of this feature are less than 30. GLCM, Gray Level Co-occurrence Matrix; GLRLM, Gray Level Run Length Matrix; GLSZM, Gray Level Size Zone Matrix; Idmn, Inverse Difference Moment Normalized; Idn, Inverse Difference Normalized; Id, Inverse Difference; Idm, Inverse Difference Moment; Imc1, InformationMeasureCorr1; Imc2, InformationMeasureCorr2.

cirrhotic sample. In *Figure 4C*, the 3D vessel microstructure of HCC is shown. Obvious distortion of the main stem is detected in spite of the vessel walls being smooth.

Quantitative assessment of liver parenchyma

For each VOI from the ILPCI-CT 3D images, 74 radiomic feature measurements were calculated. In *Figure 5*, for each feature, the %COV value is presented. The correspondence between the numbers and features is shown on the right. In total, 38 (approximately 51%) radiomic features had low variation (%COV <30), including 11 first order features, 16 GLCM features, 6 GLRLM features and 5 GLSZM features. All of the low variation radiomic features can be found in *Figure 5* with italic and bold fonts. As illustrated in *Figure 6*, statistical analysis showed significant differences among the three groups for 3 radiomic features (first-order entropy, GLCM-inverse variance and GLCM-sum entropy).

Quantitative assessment of the microvasculature

The mean vessel branch angle values of the healthy, cirrhotic and HCC samples were 65.1°, 88.9° and 100.3°, respectively. This parameter showed a statistically significant difference among the three groups ($P<0.05$).

Discussion

Medical imaging is considered as one of the fundamental building blocks of clinical hepatology. It is routinely used for liver diagnosis, treatment planning, and treatment response monitoring. Conventional X-ray imaging relies on differences in linear attenuation coefficients between tissues to produce differences in photon fluence incident upon the detector. However, these differences are usually small between different types of soft tissue and thus lead to an inherent low contrast. PCI exploits a contrast mechanism based on differences in the X-ray refractive index

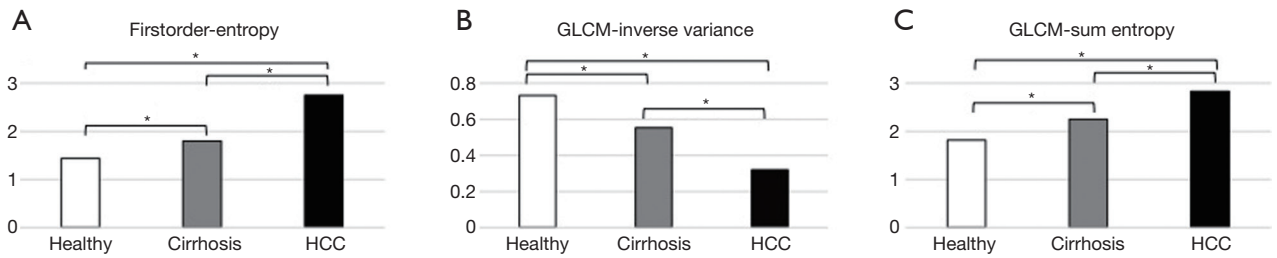

Figure 6 Three radiomic features showed significant differences in three groups. *, represents statistically significant between the two groups.

distribution of an object, which is more sensitive to relative differences between materials at diagnostic X-ray energies than is the absorption contrast mechanism. Therefore, PCI has an advantage in observing the microstructures of biological soft tissues.

ILPCI is the simplest and fastest PCI technique. In this report, we presented an *ex vivo* study of ILPCI-CT for human healthy liver, cirrhotic liver and HCC without any contrast agent. The ILPCI-CT 3D images showed texture and density changes in cirrhotic liver and HCC samples with respect to healthy liver tissue. The 3D reconstruction technique provided an excellent view of microvascular details that were invisible on conventional radiography.

In our previous study, ILPCI-CT yielded high-resolution micro-CT images of a benign solid tumor [a cavernous hemangioma of the liver (CHL)] at the micron scale (26). Additionally, 3D structures of an abnormal and dilated hepatic sinusoid were detected clearly (26). Using qualitative descriptions and quantitative measurement of microvessels in diffraction-enhanced imaging CT (DEI-CT), we could identify different stages of hepatic fibrosis (27). In addition, a thrombus inside the vessel of a severely fibrotic liver was accurately displayed, and corresponding analysis could provide an exact measurement of the vessel stenosis rate (27). In PCI experiments of human HCC, Jian *et al.* (30) found that fine structures of the microvasculature and thrombi in tiny blood vessels could be displayed clearly on images of HCC tissues by ILPCI-CT. Moreover, they found that the density distributions of the thrombi could be reliably used to distinguish malignant from benign thrombi in HCC. In another study (31), they found alterations of capillarized sinusoids, and a trabecular structure could be clearly observed in 3D geometry using ILPCI-CT, corresponding to information on actual structures revealed on histological sections. The 3D qualitative analyses showed that sinusoids in the high-grade HCC group were significantly different ($P<0.05$) in the percentage of sinusoidal area (PSA) (7.8%±2.5%) and sinusoidal volume [$(2.9\pm0.6)\times10^7$ μm^3] from those in the low-grade HCC group [PSA, 12.9%±2.2%; sinusoidal volume, $(2.4\pm0.3)\times10^7$ μm^3]. Moreover, the 3D quantitative evaluation of the trabecular structure in the high-grade HCC group showed a significant change ($P<0.05$) in the trabecular thickness (87.8±15.6 μm) and surface-area-to-volume ratio (SA/V) [$(2.2\pm1.3)\times10^3$ μm^{-1}] compared to the low-grade HCC group [trabecular thickness, 75.9±7.1 μm; SA/V, $(7.5\pm1.3)\times10^3$ μm^{-1}]. Li *et al.* (32) utilized X-ray DEI for diagnosing hepatic fibrosis. The refraction contrast images of fibrotic rat liver samples clearly showed abnormal liver architecture compared with the architecture of normal rat liver samples. In addition, to identify different degrees of liver fibrosis, quantitative analyses of texture features in each refraction image were performed using a gray level co-occurrence matrix method. They found quantitative texture analysis showed good sensitivity and specificity for texture features of normal tissue and in different stages of fibrosis. In an ILPCI experiment of nude mouse hepatic tumors, Tao *et al.* detected (33) the morphological and density changes in early hepatic tumors. The results showed that normal regions and diseased regions in the projection image could be distinguished using quantitative texture analysis.

However, one hypothesis is that 2D projection thickness of the sample due to different rotation angles leads to variable texture analysis results, especially in the case of limited specimen size. In fact, the best way to avoid the influence of tissue thickness is to perform the experiment on ILPCI-CT 3D images. To provide consistent, nonbiased descriptors of liver parenchyma images, quantitative image features (radiomic features) were extracted from ILPCI-CT 3D images in this study. Furthermore, we evaluated the stability of each radiomic feature by evaluating the COV%. It is worth noting that our results indicated approximately

51% of the quantitative imaging features showed stability. This is in disagreement with findings by Li *et al.* (32) and Tao *et al.* (33). They found most features were sensitive and specific for hepatic fibrosis and hepatic tumors in rats. It should also be mentioned that their texture analysis results from 2D projection images may be influenced by the samples' projection angles. Different from their research, we extracted more quantitative imaging features from ILPCI-CT 3D images and avoided the influence of tissue thickness.

As an image preprocessing operation, phase retrieval is a technique for obtaining quantitative phase information in PCI, and it can provide more detailed information of the sample. However, as described in a previous report (34), radiomic feature quantification can be sensitive to a number of technical factors. The phase retrieval operation may affect radiomic feature quantification. Although many phase retrieval algorithms have been proposed utilizing single- and multi-SDD(s) PCI-CT data (35-37), the use of various algorithms may lead to different quantitative results. In addition, we found ILPCI-CT without phase retrieval could also supply clear imaging results. Therefore, instead of phase retrieval images, the original projection images were applied in our experiment to avoid the above influences.

In this study, we found two radiomic features (first-order entropy and GLCM-sum entropy) with values that consistently were larger and one radiomic feature (GLCM-inverse variance) value that consistently decreased from healthy liver to cirrhotic liver and to HCC. Mathematically, entropy reflects the degree of randomness for an area. A large value of entropy means high image complexity. Inverse variance is a parameter that reflects the regular degree of texture. A small value for inverse variance means high irregularity. It is well-known that cirrhosis is characterized by fibrosis and nodule formation. Meanwhile, the liver cells lose normal alignment. Different from healthy liver and cirrhotic liver, HCC is highly heterogeneous with many hypoxic, necrotic, and high metabolic areas. This would imply that the liver texture also becomes more complex in the multistep process from a healthy liver to a cirrhotic liver and then to HCC. To some extent, these phenomena may perhaps explain our study results about quantitative assessment of the liver parenchyma.

We also observed that vessel branch angles were a useful metric to quantify vessel pathology for healthy liver, cirrhotic liver, and HCC. It has long been considered that cirrhosis is a vascular disease of the liver, owing to the marked anatomic changes that occur in the intrahepatic circulation (38). We found the mean vessel branch angles in cirrhotic liver were closer to 90°. The causes may mainly be ascribed to the formation of pseudolobules and fiber septa, inflammation and collagen proliferation. Different from cirrhosis, arterial blood and neovascularization are the primary blood sources in HCC. Neovascularization can continue unchecked due to histanoxia. This might explain why the vessel branch angles in this study were unusually large in the HCC samples.

Theoretically, the volumes of the hepatic lobule, pseudolobuli and tubercle in humans are much larger than in rats. Because we used small imaging fields of view, we may not have observed them. In future research, we will extend the study to incorporate large field view imaging for human samples using image stitching technology. Additional future studies are also warranted to investigate the sensitivity and specificity for the detection of cirrhosis and HCC. We also expect to acquire anatomical information and iron deposition information from PCI-CT and fluorescence CT of the same liver specimen. We will investigate the relativity and complementarity between the two types of images in order to obtain more information about cirrhosis and HCC.

Conclusions

In conclusion, we focused on detecting variations in liver parenchyma and microvasculature on ILPCI-CT for healthy liver, cirrhotic liver and HCC. Different from prior studies, we employed human samples instead of animal samples. In addition, healthy liver and cirrhotic liver experiments were incorporated in this research, which have been rarely investigated in previous studies. Furthermore, we quantitatively assessed the liver parenchyma using advanced imaging features that were extracted from ILPCI-CT 3D images. To some extent, this study overcame the insufficiency caused by the sample thickness.

Acknowledgments

The authors would like to thank the staffs from beamline BL13W1 of SSRF, China, for their kindly assistance in our experiments.

Funding: This research was supported by the National Key Research and Development Program of China (No. 2017YFC0113202) and the WBE Liver Fibrosis Foundation, China (Grant No. CFHPC2019027) and the Shandong Natural Science Foundation (No. ZR2017PH071).

Footnote

Conflicts of Interest: The authors have no conflicts of interest to declare.

Ethical Statement: The study was approved by Tianjin Medical University Cancer Institute and Hospital ethics committee (No. E2010391). Written informed consent was obtained from all patients.

References

1. Siegel RL, Miller KD, Jemal A. Cancer statistics, 2016. CA Cancer J Clin 2016;66:7-30.
2. McGlynn KA, London WT. Epidemiology and natural history of hepatocellular carcinoma. Best Pract Res Clin Gastroenterol 2005;19:3-23.
3. Rinninella E, Zocco MA, De Gaetano A, Iezzi R, Campanale M, Cesario V, Barbaro F, Ponziani FR, Caracciolo G, Triarico S, Tortora A, Ianiro G, Gasbarrini A. From small nodule to overt HCC: a multistep process of carcinogenesis as seen during surveillance. Eur Rev Med Pharmacol Sci 2012;16:1292-4.
4. Forner A, Vilana R, Ayuso C, Bianchi L, Solé M, Ayuso JR, Boix L, Sala M, Varela M, Llovet JM, Brú C, Bruix J. Diagnosis of hepatic nodules 20 mm or smaller in cirrhosis: prospective validation of the noninvasive diagnostic criteria for hepatocellular carcinoma. Hepatology 2008;47:97-104.
5. Sumida Y, Nakajima A, Itoh Y. Limitations of liver biopsy and non-invasive diagnostic tests for the diagnosis of nonalcoholic fatty liver disease/nonalcoholic steatohepatitis. World J Gastroenterol 2014;20:475-85.
6. Dai Y, Chen MH, Fan ZH, Yan K, Yin SS, Zhang XP. Diagnosis of small hepatic nodules detected by surveillance ultrasound in patients with cirrhosis: Comparison between contrast-enhanced ultrasound and contrast-enhanced helical computed tomography. Hepatol Res 2008;38:281-90.
7. Takeda T, Momose A, Itai Y, Wu J, Hirano K. Phase-contrast imaging with synchrotron X-rays for detecting cancer lesions. Acad Radiol 1995;2:799-803.
8. Pfeiffer F, Herzen J, Willner M, Chabior M, Auweter S, Reiser M, Bamberg F. Grating-based X-ray phase contrast for biomedical imaging applications. Z Med Phys 2013;23:176-85.
9. Bravin A, Coan P, Suortti P. X-ray phase-contrast imaging: from pre-clinical applications towards clinics. Phys Med Biol 2013;58:R1-35.
10. Wang B, Zhang B, Huo H, Wang T, Wang Q, Wu Y, Xiao L, Ren Y, Zhang L. Detection of microvasculature alterations by synchrotron radiation in murine with delayed jellyfish envenomation syndrome. Toxicon 2014;81:48-53.
11. Momose A, Takeda T, Itai Y, Hirano K. Phase-contrast X-ray computed tomography for observing biological soft tissues. Nat Med 1996;2:473-75.
12. Xuan R, Zhao X, Hu D, Jian J, Wang T, Hu C. Three-dimensional visualization of the microvasculature of bile duct ligation-induced liver fibrosis in rats by x-ray phase-contrast imaging computed tomography. Sci Rep 2015;5:11500.
13. Qin L, Zhao X, Jian J, Zhao Y, Sun M, Hu C. High-resolution 3D visualization of ductular proliferation of bile duct ligation-induced liver fibrosis in rats using x-ray phase contrast computed tomography. Sci Rep 2017;7:4215.
14. Töpperwien M, van der Meer F, Stadelmann C, Salditt T. Three-dimensional virtual histology of human cerebellum by X-ray phase-contrast tomography. Proc Natl Acad Sci USA 2018;115:6940-5.
15. Barbone GE, Bravin A, Romanelli P, Mittone A, Bucci D, Gaaβ T, Le Duc G, Auweter S, Reiser MF, Kraiger MJ, Hrabě de Angelis M, Battaglia G, Coan P. Micro-imaging of Brain Cancer Radiation Therapy Using Phase-contrast Computed Tomography. Int J Radiat Oncol Biol Phys 2018;101:965-84.
16. Massimi L, Fratini M, Bukreeva I, Brun F, Mittone A, Campi G, Spanò R, Mastrogiacomo M, de Rosbo NK, Bravin A, Uccelli A, Cedola A. Characterization of mouse spinal cord vascular network by means of synchrotron radiation X-ray phase contrast tomography. Phys Med 2016;32:1779-84.
17. Liao S, Ni S, Cao Y, Yin X, Wu T, Lu H, Hu J, Wu H, Lang Y. The 3D characteristics of post-traumatic syringomyelia in a rat model: a propagation-based synchrotron radiation microtomography study. J Synchrotron Radiat 2017;24:1218-25.
18. Cao Y, Zhou Y, Ni S, Wu T, Li P, Liao S, Hu J, Lu H. Three dimensional quantification of microarchitecture and vessel regeneration by synchrotron radiation microcomputed tomography in a rat model of spinal cord injury. J Neurotrauma 2017;34:1187-99.
19. Zhang L, Li D, Luo S. Non-invasive microstructure and morphology investigation of the mouse lung: qualitative description and quantitative measurement. PLoS One 2011;6:e17400.
20. Yi E, Han SM, Chang JE, Kim HT, Kim JK, Seo SJ, Chung JH, Jheon S. Synchrotron tomographic images

from human lung adenocarcinoma: Three-dimensional reconstruction and histologic correlations. Microsc Res Tech 2017;80:1141-8.
21. Gu S, Xue J, Xi Y, Tang R, Jin W, Chen J, Zhang X, Shao Z, Wu J. Evaluating the effect of Avastin on breast cancer angiogenesis using synchrotron radiation. Quant Imaging Med Surg 2019;9:418-26.
22. Li B, Zhang Y, Wu W, Du G, Cai L, Shi H, Chen S. Neovascularization of hepatocellular carcinoma in a nude mouse orthotopic liver cancer model: a morphological study using X-ray in-line phase-contrast imaging. BMC Cancer 2017;17:73.
23. Liu H, Ji X, Sun L, Xiao T, Xie H, Fu Y, Zhao Y, Liu W, Zhang X, Lin R. Visualization and Pathological Characteristics of Hepatic Alveolar Echinococcosis with Synchrotron-based X-ray Phase Sensitive Micro-tomography. Sci Rep 2016;6:38085.
24. Fu Y, Peng H, Zhang X, Peng W, Wu J, Wang S, Du M, Li R. Assessment of fibrotic tissue and microvascular architecture by in-line phase-contrast imaging in a mouse model of liver fibrosis. Eur Radiol 2016;26:2947-55.
25. Velroyen A, Bech M, Zanette I, Schwarz J, Rack A, Tympner C, Herrler T, Staab-Weijnitz C, Braunagel M, Reiser M, Bamberg F, Pfeiffer F, Notohamiprodjo M. X-ray phase-contrast tomography of renal ischemia-reperfusion damage. PLoS One 2014;9:e109562.
26. Duan J, Hu C, Chen H. High-resolution micro-CT for morphologic and quantitative assessment of the sinusoid in human cavernous hemangioma of the liver. PLoS One 2013;8:e53507.
27. Duan J, Hu C, Luo S, Zhao X, Wang T. Microcomputed tomography with diffraction-enhanced imaging for morphologic characterization and quantitative evaluation of microvessel of hepatic fibrosis in rats. PloS One 2013;8:e78176.
28. Korn A, Fenchel M, Bender B, Danz S, Hauser TK, Ketelsen D, Flohr T, Claussen CD, Heuschmid M, Ernemann U, Brodoefel H. Iterative reconstruction in head CT: image quality of routine and low-dose protocols in comparison with standard filtered back-projection. AJNR Am J Neuroradiol 2012;33:218-24.
29. Shafiq-Ul-Hassan M, Zhang GG, Latifi K, Ullah G, Hunt DC, Balagurunathan Y, Abdalah MA, Schabath MB, Goldgof DG, Mackin D, Court LE, Gillies RJ, Moros EG. Intrinsic dependencies of CT radiomic features on voxel size and number of gray levels. Med Phys 2017;44:1050-62.
30. Jian J, Yang H, Zhao X, Xuan R, Zhang Y, Li D, Hu C. Visualization of microvasculature and thrombi by X-ray phase-contrast computed tomography in hepatocellular carcinoma. J Synchrotron Radiat 2016;23:600-5.
31. Jian J, Zhang W, Yang H, Zhao X, Xuan R, Li D, Hu C. Phase-contrast CT: Qualitative and Quantitative Evaluation of Capillarized Sinusoids and Trabecular Structure in Human Hepatocellular Carcinoma Tissues. Acad Radiol 2017;24:67-75.
32. Li H, Zhang L, Wang X, Wang T, Wang B, Zhao X, Luo S. Investigation of hepatic fibrosis in rats with x-ray diffraction enhanced imaging. Appl Phys Lett 2009;94:124101.
33. Tao Q, Li D, Zhang L, Luo S. Using x-ray in-line phase-contrast imaging for the investigation of nude mouse hepatic tumors. PLoS One 2012;7:e39936.
34. Yip SS, Aerts HJ. Applications and limitations of radiomics. Phys Med Biol 2016;61:R150-66.
35. Weitkamp T, Haas D, Wegrzynek D, Rack A. ANKAphase: software for single-distance phase retrieval from inline X-ray phase-contrast radiographs. J Synchrotron Radiat 2011;18:617-29.
36. Chen RC, Dreossi D, Mancini L, Menk R, Rigon L, Xiao TQ, Longo R. PITRE: software for phase-sensitive X-ray image processing and tomography reconstruction. J Synchrotron Radiat 2012;19:836-45.
37. Häggmark I, Vågberg W, Hertz HM, Burvall A. Comparison of quantitative multi-material phase-retrieval algorithms in propagation-based phase-contrast X-ray tomography. Optics Express 2017;25:33543-58.
38. Bosch J. Vascular deterioration in cirrhosis: the big picture. J Clin Gastroenterol 2007;41:S247-S253.

Cite this article as: Duan J, Hu C, Qiu Q, Zhang J, Meng H, Wang K, Dong H, Wei H, Yin Y. Characterization of microvessels and parenchyma in in-line phase contrast imaging CT: healthy liver, cirrhosis and hepatocellular carcinoma. Quant Imaging Med Surg 2019;9(6):1037-1046. doi: 10.21037/qims.2019.06.12

